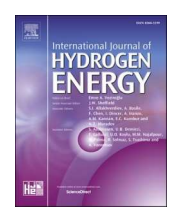
ELSEVIER

Contents lists available at ScienceDirect

International Journal of Hydrogen Energy

journal homepage: www.elsevier.com/locate/he





Synthesis of defect-engineered molybdenum sulfides on reduced graphene oxide for enhanced hydrogen evolution reaction kinetics

Archana Sekar, Kamalambika Muthukumar, Sabari Rajendran, Jun Li

Department of Chemistry, Kansas State University, Manhattan, KS, 66506, USA

ARTICLE INFO

Handling editor: E.A. Veziroglu

Keywords:
Molybdenum sulfide
Hydrogen evolution reaction
Electrocatalyst
Defect engineering
Hybrid materials

ABSTRACT

Amorphous molybdenum sulfide (a-MoS₃) is a promising non-precious electrocatalyst for hydrogen evolution reaction owing to the abundant defective active sites. Here in, we show a rapid microwave-assisted synthesis method to produce a-MoS₃ catalysts on reduced graphene oxide (rGO) substrates. The a-MoS₃ reported in this study comprise of two possible 1D chain-like structures, i.e., with molybdenum (IV) in Weber's model and molybdenum (V) in Hibble's model, unlike the polymeric cluster type a-MoS₃ structures reported in literature. Thermal annealing of the microwave-prepared a-MoS₃ produced a family of defect-engineered MoS_x/rGO hybrids, from a-MoS₃ to crystalline MoS₂, which showed tunable HER activities. XPS analysis provided in-depth understanding of the compositional changes in MoS_x/rGO with thermal annealing. The a-MoS₃/rGO 250 (annealed at 250 °C) exhibited the highest HER catalytic activity among all the MoS_x/rGO hybrids, with an overpotential of 208 mV at 10 mA/cm², a low Tafel slope of 52 mV/decade, a high double layer capacitance of 3.7 mF/cm² and a high TOF value of 0.43 H₂/s per site at the HER overpotential of 208 mV. The excellent HER activity is attributed to both MoV and sulfur active sites. This study provides a controllable, scalable and rapid synthesis method to produce 1D chain-like a-MoS₃ structures for HER electrocatalysis.

1. Introduction

The depletion of fossil fuel has created an ever-increasing demand for alternate energy sources. Hydrogen is a promising energy carrier in transportation sectors owing to its high gravimetric energy density (~120 MJ/kg) in compressed gas form [1,2]. More than 95% of today's hydrogen is produced by steam methane reforming and coal gasification, leading to enormous carbon emissions. In addition, the exponential growth of global hydrogen demand pushes for the increasing need to reduce carbon emission [1,3]. Hence, the development of a renewable and green technology to produce hydrogen is essential for sustainable hydrogen economy. Water electrolyzer is the best zero-carbon emission alternative technology for green hydrogen gas production by splitting water using electricity (generated from renewable sources such as solar panels and wind turbines). The green hydrogen gas produced in this way has the highest purity of about 99.999% [1].

In proton exchange membrane water electrolyzers (PEMWEs), hydrogen is produced by the hydrogen evolution reaction (HER) at the cathode compartment [4]. In an acidic electrolyte, the protons are reduced to hydrogen following the equation given below, with the

standard reduction electropential $E^0=0V$ vs. the standard hydrogenelectrode (SHE):

$$2H^{+} + 2e^{-} \longrightarrow H_{2}$$
 (1)

The state-of-the-art catalyst for HER is platinum (Pt). It is well known that Pt is at the top of the volcano plot and has a negligible overpotential for HER due to the optimal hydrogen adsorption Gibbs free energy ($\Delta G_{\rm H} = \sim 0$ eV) [4]. Due to the high cost of Pt, the economic scale up of PEMWEs technology is challenging. At an annual production rate of 1000 units/year, the catalyst coated membrane (CCM) of 1 MW PEMWE stack accounts for 35% - 50% of the cost of electrolyzer stacks [5]. Recently, the U.S. Department of Energy's first energy earth shot program has announced a target to reduce the cost of green $\rm H_2$ by 80 % to \$1/kg in a decade in order to realize the hydrogen economy [6]. As a result, the need for less expensive, earth-abundant alternatives to Pt as the HER catalyst has driven the exploration of numerous catalysts based on non-precious metals.

Among various non-precious HER electrocatalysts [7], transition metal dichalcogenides such as molybdenum sulfides (MoS_x), tungsten sulfides (MoS_y), molybdenum selenides (MoS_y), tungsten selenides

^{*} Corresponding authors.

E-mail address: junli@ksu.edu (J. Li).

(WSe₂) have shown compelling HER electrocatalytic activity [8–11]. Amongst them, molybdenum sulfides (MoSx) have acquired special interests in acidic electrolytes owing to their good stability in low-pH electrolytes compared to other transition metals [12,13]. MoS_x exists in crystalline, amorphous and molecular cluster forms [14]. The two-dimensional (2D) trilayered 2H crystalline MoS₂ structure (c-MoS₂) was the first one that gained attention as HER electrocatalyst owing to the similarity of its edge site structure to nitrogenase and hydrogenase. the natural hydrogen producing enzymes, and the proper hydrogen adsorption Gibbs free energy at the edge sites ($\Delta G_H = 0.08$ eV) that is comparable to Pt metal [7,15]. However, experimental HER activity of c-MoS $_2$ was substantially lower than that of Pt, as reflected in the orders of magnitude lower exchange current density, due to the very low density of exposed active edge sites and the dominance of inactive basal planes [13,16]. In order to improve the HER activity, several research groups reported strategies to control the size, morphology and number of stacked layers of c-MoS2, enhance exposed edge sites by creating sulfur vacancies, or activate the basal plane with new active sites by incorporating dopant atoms [16-20]. Other approaches, such as chemical exfoliation to form nanosheets, and formation of nanoparticles and nanowires with a high density of active edge sites were also explored [13,21-24]. Nevertheless, increasing the active site density of the 2D c-MoS₂ structure was challenging and the HER activity remains far below that of Pt catalysts.

On the other hand, a set of amorphous MoSx materials (with x varying between 2 and 3), commonly called a-MoS_x or simply a-MoS₃, have attracted special attention due to their disordered and defect-rich structure [16]. They have shown enhanced HER activities compared to the bulk c-MoS₂ counterparts [12]. In contrast to the 2D layered c-MoS₂, a-MoS₃ was found to have amorphous 1D chain-like nanostructures, with abundantly exposed bridging S_2^{2-} , terminal S_2^{2-} , unsaturated S²⁻, and apical S²⁻ ligands [25,26]. However, the structure of a-MoS₃ still remains a debating topic due to the lack of convincing structural characterization techniques for amorphous materials. Their structures depend on materials synthesis methods and are sensitive to the experimental conditions, making it even more difficult to study. The simplest models for a-MoS₃ are two types of chain-like structures consisting of triangular dipyramidal units that were proposed by Hibble et al. [27] and Weber et al. [26], respectively. Hibble's a-MoS₃ structure formula is given as $\text{Mo}^{\text{V}}(S^{2-})_2(S^{2-}_2)_{0.5}$, in which two sets of S_3 ligands, one set consisting of three sulfides (S^{2-}) and the other set consisting of one sulfide (S^{2-}) and one disulfide (S^{2-}), alternately bridge the two neighboring Mo(V) centers in the apexes of the triangular dipyramidal units in the chain (see later in Fig. 3(d)) [27]. In contrast, Weber's a-MoS₃ structure presents the formula of $Mo^{IV}(S^{2-})(S_2^{2-})$, in which all molybdenum(IV) apex centers are bridged by the similar set of S3 ligands consisting of one sulfide (S^{2-}) and one disulfides (S_2^{2-}) (see later in Fig. 3(e)) [26]. More complicated polymeric a-MoS_x structures consisting of trinuclear [Mo₃S₁₃]²- clusters were also extensively reported, mostly based on electrochemically deposited a-MoS₃ [28–31]. Several research groups also explored molecular sulfido clusters (such as dinuclear $[\text{Mo}_2^{\text{V}} S_{12}]^{2-}$ and trinuclear $[\text{Mo}_3^{\text{IV}} S_{13}]^{2-})$ [32] as molecular analogues of a-MoS $_3$ and achieved low Tafel slopes of \sim 40 mV/decade that are close to that of Pt/C (~30 mV/decade) [33]. Despite of the complexity of the structures, all a-MoSx catalysts have shown substantial enhancement in HER catalytic activity than c-MoS₂.

Hu and co-workers were the first group to investigate a-MoS₃ thin films on glassy carbon electrodes (GCE) by anodic electrodeposition using $(NH_4)_2(MoS_4)$ in 0.1 M NaClO₄ and reported a HER overpotential of 200 mV at 5 mA/cm² with a turnover frequency (TOF) value of 0.23H₂/s per site [12]. The abundant S₂² sites were suggested to be the active sites for the enhanced HER activity. In a later study, they carried out deeper materials characterization by in-situ X-ray absorption spectroscopy (XAS) and X-ray photoelectron spectroscopy (XPS)

experiments, and suggested that protons bind to the terminal S_2^{2-} ligands of the sophisticated a-MoS_x structure which led to H₂ generation [28]. However, using operando Raman spectroscopy and density functional theory (DFT) studies, Yeo et al. revealed that the bridging S₂²⁻ ligands are the active sites for HER rather than the terminal S_2^{2-} based on observation of the S-H stretching vibration of MoSx-H moieties in Raman spectra and the low ΔG_H of protons at bridging S_2^{2-} compared to terminal S_2^{2-} [29,30]. In contrast to this, Tran et al. reported the formation of Mo^V-H moiety during HER in the [Mo₃S₁₃]²- building blocks of electrochemically deposited a-MoS_x, and suggested MoV to be the active species to produce hydrogen [31]. This MoV-based mechanism was supported by a few other studies [34,35]. Li et al. attributed the high catalytic activity of the a-MoS $_{\rm x}$, synthesized by laser ablation method, to the increased density of Mo^V defect sites and bridging S_2^{2-} ligands [35]. Anyways, the HER mechanism and origin of active sites in a-MoS_x are still not well understood and require further studies. On this note, the a-MoS_x employed for HER electrocatalysis in reports are synthesized by electrodeposition [12,28], space-confined calcinated strategy [14], liquid phase/wet-chemical synthesis [16], femtosecond laser ablation [35], ultrasonic spray pyrolysis [36], and hydrothermal synthesis [37]. These reported methods are unscalable, time consuming, energy intensive, or have limited control in the defect density. Hence, there remains a considerable demand for developing a rapid and scalable synthesis method for a-MoS_x with abundant active sites for HER. Ideally, the ability to produce a series of MoS_x materials with the tunable structures from a-MoS₃ to c-MoS₂ is useful for systematic comparison to identify the optimal HER catalyst.

In addition, despite the attractive electrocatalytic activity of a-MoS $_{\rm X}$ towards HER, it has a low electronic conductivity resulting in inefficient charge transport that may impede the practical utilization. An approach to overcoming this is to form hybrid structures of a-MoS $_{\rm X}$ on electrically conductive carbon templates, such as porous carbon [38], carbon nanotubes [39], carbon nanofibers [40] and reduced graphene oxide (rGO) [41–43] to improve the electron transport. Among these materials, rGO is widely studied owing to the ability to deposit well dispersed MoS $_{\rm X}$ nanostructures with abundant HER active edge sites on the 2D rGO planes that possess a high specific surface area (SSA).

Here in, we report a simple, controllable, and rapid microwaveassisted synthesis to prepare amorphous a-MoS3 on a rGO template as a HER electrocatalyst. Due to the hydrothermal conditions in microwave process (high pressureand above 100 °C), the as-synthesized a-MoS₃/ rGO showed Raman spectra distinct from the polymeric a-MoS_x clusters reported in literature and can be well explained by an approximately equal mixture of amorphous Hibble and Weber MoS₃ 1D chain structures. Subsequent thermal annealing of the microwave-synthesized a-MoS₃/rGO at various temperatures in a mixed gas of 3% H₂ and 97% Ar produced a family of defect-engineered MoS_x/rGO hybrids with a tunable S to Mo ratio from 3.6 to 2.2. By annealing at 250 °C, the obtained catalyst (a-MoS₃/rGO 250) showed a higher composition of Weber type of a-MoS₃. While annealing at 325 °C (referred to as a-MoS_x/ rGO 325), a portion of a-MoS₃ was converted into c-MoS₂. At 600 °C, all a-MoS₃ was converted into crystalline c-MoS₂ nanopatches (referred to as c-MoS₂/rGO 600). XPS analysis provided in-depth understanding of the compositional changes from a-MoS₃ to c-MoS₂ as the annealing temperature was raised. All a-MoS₃/rGO catalysts outperformed the c-MoS₂/rGO 600 even though the latter contained abundant edge sites due to the formation of the c-MoS₂ nanopatches (~4.4 nm dia. and 4.2 nm in thickness). The a-MoS₃/rGO 250 exhibited the highest HER catalytic activity, with an overpotential of 208 mV at 10 mA/cm², a low Tafel slope of 52 mV/decade, a high double layer capacitance of 3.7 mF/cm² and a high TOF value of 0.43H₂/s per site at the HER overpotential of 208 mV. This synthesis method can be further improved to prepare the optimal a-MoS₃/rGO hybrids for future HER electrocatalysis.

2. Materials and methods

2.1. Chemicals and materials

Ammonium tetrathiomolybdate (NH₄)₂MoS₄ (ATM), tetrahydrofuran (THF), and Nafion® solution (5 wt% in lower aliphatic alcohols) were purchased from Sigma-Aldrich (St. Louis, MO). The single-layer graphene oxide (GO) flakes were purchased from ACS Material LLC (Pasadena, CA). Sulfuric acid (H₂SO₄) and pure ethanol 200 proof were purchased from Fisher Scientific (Hampton, NH). Ultrapure water (18.2 $\rm M\Omega$ cm at 25 °C) purified from a Millipore water system (EASYPURE II, Thermo Scientific, Waltham, MA) was used to prepare all aqueous solutions for the experiments. The commercial Pt/C catalyst (20 wt% Pt on carbon, HiSPEC® 3000) by Johnson Matthey (JM) was purchased from Alfa Aesar (Tewksbury, MA) to use as the benchmark reference.

2.2. Materials synthesis

15.0 mM ATM and 5.0 mg of GO were mixed and sonicated in a mixture of 6.0 mL of THF and 1.0 mL of water for 20 min. This mixture was irradiated with microwaves (Discover SP, CEM Corp., Mathews, NC) in a dynamic mode at 170 °C for 10 min. The reaction pressure rose to $\sim\!\!21$ bar. These hydrothermal conditions (high pressure and above 100 °C) yielded products distinct from those by typical wet-chemical synthesis or electrodeposition. The microwave-synthesized sample was then centrifuged to collect the solid product, which was dried on a hotplate at $\sim\!\!80$ °C overnight to obtain the intermediate material (denoted as a-MoS₃/rGO int). The dried intermediate material was then annealed in 3% H₂/97% Ar atmosphere at 250 °C, 325 °C and 600 °C, respectively, for 2 h following a ramp rate of 10 °C/min. These samples were denoted as a-MoS₃/rGO 250, MoS_x/rGO 325 and c-MoS₂/rGO 600, respectively.

2.3. Materials characterization

The catalyst morphology was characterized using a Philips CM 100 transmission electron microscope (TEM) at a 100 kV acceleration voltage. The crystal structure of the catalysts was examined using Bruker AXS D8 Advance Diffractometer (Bruker Corporation, Karlsruhe, Germany) with a Cu K α radiation of wavelength 0.15418 nm and a detector slit width of 1 mm. XRD reference spectra from Joint Committee on Powder Diffraction Standards (JCPDS) were used. The Raman spectroscopic measurements were performed with a DXR Raman microscope (Thermo fisher Scientific, Madison, WI)) with a 532 nm laser at the power of 5 mW, under a $10 \times$ objective lens with a slit width of 25 μ m. The surface chemical composition of the catalysts was characterized using a PHI 5000 Versa XPS system (Chanhassen, MN) with a monochromatized Al Ka source (1486.7 eV) at University of Nebraska, Lincoln. All the XPS spectra were obtained using a 400 µm spot size. The binding energy (B.E.) of all XPS data was calibrated vs. the standard C 1s peak at 284.60 eV before the curve fitting. Shirley background was used in the curve fitting. We fit the Mo 3d and S 2p XPS spectra using a rigorous procedure by fixing spin-orbital splitting energy and area ratio at appropriate standard values. Elemental analyses of the atomic percentage (at%) of C, H, N and S were acquired using a PE 2100 Series II combustion analyzer (PerkinElmer Inc., Waltham, MA) at Iowa State University. The combustion tube packing was supplied with the instrument and consisted of the following components: copper oxide wires and electrolytic copper was used for CHNS reduction, and the oxygen reduction tube was packed with nickel plated carbon and quartz turnings. Vanadium pentoxide was used as combustion aid for sulfur analysis. The compounds were sampled using pressed tin capsules for CHNS Analysis and silver capsules for O analysis. 2,5-Bis(5-tert-butyl-benzoxazol-2-yl) thiophene was used as the calibration standard for all the samples unless notified otherwise in the discussion. The combustion and reduction temperature for CHNS analysis were 975 °C. All the standards

and reagents were purchased from PerkinElmer or Elemental America's Inc. The precision and accuracy of the results were estimated to be as low as $\pm 0.3\%$.

2.4. Electrochemical characterization

All the half-cell electrochemical experiments were performed in a standard three-electrode setup using a CHI 760D electrochemical workstation (CH Instruments, Austin, TX) at room temperature in Arpurged 0.50 M H₂SO₄ electrolyte throughout the study. A mercury/ mercurous sulfate reference electrode (MSE, Hg/Hg₂SO₄ in saturated K₂SO₄) and a graphite counter electrode were used. The working electrode was prepared by drop-casting the catalyst ink onto a 3 mm diameter GCE. Before drop-casting the catalyst ink, the GCE was polished using $0.05 \mu m$ alumina slurry. The catalyst ink was prepared by dispersing the required amount of catalyst powder in 1.0 ml of mixture of ethanol and ultrapure water (at 3:1 vol ratio) with addition of the 30 μl of 5 wt% Nafion solution. The MoS_x/rGO loading was maintained at 125 µg/cm² for all catalysts in the half-cell studies. For direct comparison of the potentials with literature, the measured electrode potential vs. MSE reference electrode was converted to the value vs. the reversible hydrogen electrode (RHE) using the following equations:

$$E_{(vs. RHE)} = E_{(vs. MSE)} + E_{(MSE vs. SHE)} + 0.059 \text{ x pH}$$
 (2)

$$E_{(vs. RHE)} = E_{(vs. MSE)} + 0.640 V$$
 (3)

where $E_{(vs. MSE)}$ is the potential measured vs. MSE, $E_{(MSE\ vs.\ SHE)}=0.640$ V is the potential of MSE vs. SHE, and pH = 0 for 0.50 M H₂SO₄.

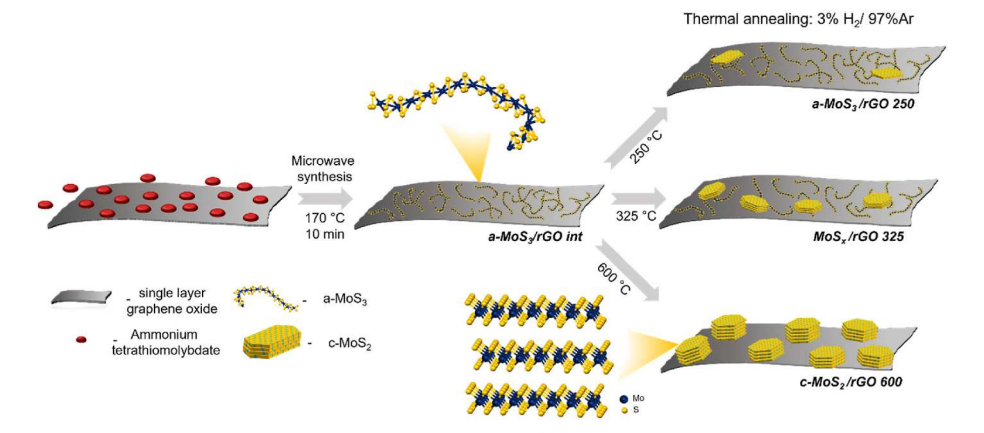
After catalyst drop-casting and subsequent drying at room temperature, the first HER polarization curve is collected by linear sweep voltammetry (LSV) in the potential range of 0.4 V to -0.4 V vs. RHE at the scan rate of 10 mV/s. The rotation of the electrode was found to have little effect on the LSV curves; thus, the main studies were carried out without rotating the electrode. In the next step, the catalysts were subjected to activation by cyclic voltammetry (CV) in the potential range of 0.4 V to -0.1 V vs. RHE at a sweep rate of 50 mV/s for 50 cycles. Then another LSV curve is collected in the potential range of 0.4 V to -0.4 V vs. RHE at 10 mV/s after the CV activation and this stabilized LSV curve is reported for HER evaluation. CV measurements in non-faradaic region at varied scan rates were done to estimate the electrical double-layer capacitance (Cdl) and electrochemical surface area (ECSA). Tafel analysis was performed to determine the kinetic parameters of the HER. The chronopotentiometry measurements were performed by fixing the current density at -10 mA/cm² for a duration of 23 h. A 100 % iR correction was done following the previous literature [44] using the following equation (4):

$$V_{iR corrected} = V_{measured} - I_{measured} x R_s$$
 (4)

where $V_{iR\ corrected}$ is the iR compensated/corrected voltage, $V_{measured}$ and $I_{measured}$ are the experimentally measured voltage and current in the LSV curve and R_s is the uncompensated solution resistance. Briefly, the iR voltage drop was calculated by multiplying the experimentally obtained current by R_s , followed by subtracting the iR voltage drop from the experimentally measured potential. The R_s was determined by fitting the electrochemical impedance spectroscopy (EIS) curves obtained for all catalysts with an appropriate equivalent circuit using ZsimpWin software. The EIS measurements were carried out from 0.8 MHz to 1000 Hz with a sinusoidal AC potential amplitude of 5 mV at the open circuit voltage (OCV).

3. Results and discussion

Scheme 1 illustrates the synthesis procedures. It is well known that the ATM precursor decomposes in inert gas atmosphere in two steps, i.e., first forming MoS_3 at $260-300\,^{\circ}C$ and then MoS_3 starting to be converted



Scheme 1. Schematic illustration of the synthesis of MoS_x/rGO hybrid materials.

to MoS_2 at the temperature above 310 °C [26]. In this study, a microwave-assisted electrocatalyst synthesis was used to selectively deposit 1D chain-like a- MoS_3 at a hydrothermal condition (170 °C and 21 bar pressure) on rGO support to form the hybrid material a- MoS_3 /rGO int, following the nominal reaction equation [26].

$$(NH4)2MoS4 \longrightarrow MoS3 + 2NH3(g) + H2S(g)$$
(5)

The low microwave absorptivity of the THF solvent (with a loss tangent value $\tan\delta=0.042$) compared to GO and rGO ($\tan\delta=0.8$ to 1.0) enabled the specific microwave heating of GO or rGO for selective deposition of MoS₃ on the carbon template. As discussed later, the a-MoS₃/rGO int material is a 1D chain-like structure with two possible forms, i.e., $\text{Mo}^{V}(\text{S}^2-)_2(\text{S}_2^2-)_{0.5}$ or $\text{Mo}^{IV}(\text{S}^2-)(\text{S}_2^2-)$ as proposed by Hibble et al. and Weber et al., respectively [26,27]. This intermediate sample was further annealed at higher temperatures of 250 °C, 325 °C and 600 °C in reducing atmosphere (3 % H₂/97 % Ar) in order to obtain different compositions that involve reduction of S₂²⁻ to S²⁻ and Mo^V to Mo^{IV}, following the equation:

$$MoS_3 + H_2 \rightarrow MoS_2 + H_2S \tag{6}$$

The annealed catalysts are denoted as a-MoS₃/rGO 250, MoS_x/rGO 325 (with x between 2 and 3) and c-MoS₂/rGO 600, with the annealing

temperature as suffix following the hybrid name. This method provided a series of MoS_x/rGO hybrid materials with the MoS_x deposit varying from a- MoS_3 to c- MoS_2 as the annealing temperature was raised.

3.1. Structural and morphological characterization

The phase and crystal structure of the four hybrid catalysts were studied using XRD as shown in Fig. S1(a) of the Supplementary Materials (SI) and Fig. 1(a). The a-MoS₃/rGO int and a-MoS₃/rGO 250 did not show any diffraction peaks, revealing the amorphous and disordered nature of MoS₃ deposited on rGO after the microwave step and the following annealing at 250 °C. This agrees with the other a-MoS₃ structures prepared by wet-chemical synthesis in literature [14,16]. But when the intermediate sample was annealed at 325 °C (MoS₂/rGO 325), broad and weak diffraction peaks at 33.09°, 38.97° and 58.44° corresponding to (100), (103) and (110) peaks of 2H-MoS₂ were observed, suggesting partial conversion of 1D a-MoS₃ to 2D crystalline 2H-MoS₂. However, the (002) plane was not observed, indicating the lack of an ordered stack of MoS2 layers. Also, (100) and (103) peaks were broad and overlapped. The domain size along (110) direction can be estimated to be only ~ 2.78 nm based on Scherrer's equation. Hence, the MoS₂ layers in MoS₂/rGO 325 are considered as small "nanopatches". The

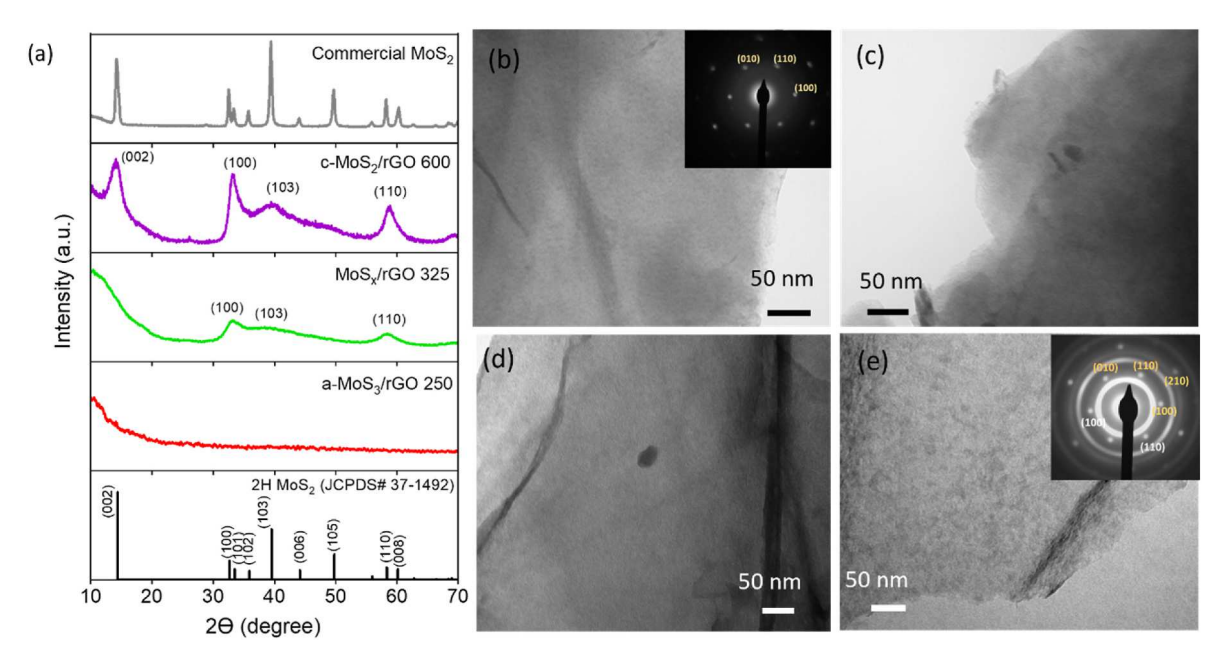


Fig. 1. (a) XRD patterns of a-MoS $_3$ /rGO 250, MoS $_x$ /rGO 325 and c-MoS $_2$ /rGO 600 compared with commercial MoS $_2$ and JCPDS data of 2H MoS $_2$. TEM image of (b) a-MoS $_3$ /rGO int, (c) a-MoS $_3$ /rGO 250, (d) MoS $_x$ /rGO 325, and (e) c-MoS $_2$ /rGO 600. The SAED patterns are shown as the inset in panels (b) and (e).

nanoscale morphology of the MoS₂ is expected to provide more exposed edge sites which are electrochemically active for HER [16].

The c-MoS₂/rGO 600 sample showed much stronger characteristic diffraction peaks at 14.15°, 33.21°, 39.42° and 58.66°, corresponding to diffraction from (002), (100), (103) and (110) planes of 2H-MoS₂. Interestingly, the 20 position of (002) plane of c-MoS₂/rGO 600 shifts to a lower 20 value (14.15° versus 14.37° of bulk 2H MoS2 crystals) and (100) plane shifts to a higher 20 value (33.21° versus 32.67° of bulk 2H MoS₂ crystals), revealing the interlayer expansion between MoS₂ layers and in-plane contraction in c-MoS₂/rGO 600 [42]. The inter layer (002) distance was found to be 6.28 Å, which was greater than 6.16 Å of bulk 2H MoS₂. Such expansion in interlayer may be due to some defective sites in the basal plane and edges of MoS2 layers. Using the Scherrer's equation, from the peak width of (002), the crystalline domain size perpendicular to the MoS₂ layer was found to be ~4.21 nm, which corresponds to \sim 7 layers of MoS₂. The MoS₂ layer domain size along (100) and (110) direction was found to be \sim 4.36 nm and \sim 4.35 nm, respectively. This further corroborates the consideration of MoS₂ as nanopatches.

Fig. S1(b) shows the TEM image of wrinkled single-layer GO flakes of a few microns in size, as the starting carbon template in this work. Fig. 1 (b)–(e) show TEM images of the four types of MoS_v/rGO hybrid structure prepared at different conditions. The MoS_x deposited on rGO flakes was quite homogeneous and difficult to be observed in TEM images owing to the nanoscale morphology and amorphous nature. Selected area electron diffraction (SAED) patterns on the a-MoS₃/rGO int (shown in inset of Fig. 1(b)), only showed sharp hexagonal diffraction spots of rGO but no patterns from the MoS2 structure, which further ascertains the amorphous structure of MoS₃ deposits in the a-MoS₃/rGO int, corroborating the XRD results. The hexagonal real-space lattice parameter was calculated to be 2.46 Å from the diffraction spots. This value matches well with the lattice parameter of graphene, indicating the successful conversion of GO into the ordered 2D crystalline rGO. In c-MoS₂/rGO 600 sample shown in Fig. 1(e), isolated darker MoS₂ nanopatches were observed on the rGO surface. Due to the low contrast, it was difficult to analyze the particle shape and size distribution using the TEM image. Interestingly, the SAED pattern of c-MoS₂/rGO 600 (the inset of Fig. 1 (e)) showed both isolated hexagonal diffraction spots of rGO and continuous rings corresponding to randomly oriented 2D MoS2 nanopatches. The first and second rings are denoted as the in-plane (100) and (110) diffractions of 2H MoS2 structure. The 2D lattice parameter of MoS₂ nanopatches was determined to be 3.16 Å, matching the hexagonal lattice of 2H MoS₂. The details of SAED calculations can be found in our previous report [42].

Fig. 2(a) and (b) show Raman spectra of the four MoS_v/rGO hybrid structures. The peaks positioned at 1348 cm⁻¹ and 1585 cm⁻¹, for all MoS_x/rGO samples, correspond to the characteristic D and G bands from the vibrations of sp³ carbon defect sites and in-plane vibration of sp² carbon of rGO, respectively [45–47]. Weak 2D band (at \sim 2700 cm⁻¹) and S3 band (at \sim 2900 cm $^{-1}$) from rGO are also observed in all four samples. The peaks observed at 376 cm⁻¹, 402 cm⁻¹ and 450 cm⁻¹ are the characteristic features of 2H MoS₂, corresponding to E_{2g}^1 vibration arising from the in-plane vibration of S atoms, A_{1g} from the out-of-plane vibration of S atoms and 2 LA (M) from edge phonons, respectively [42, 48,49]. It is interesting that only weak characteristic E_{2g}^1 and A_{1g} vibration peaks of MoS₂ present in a-MoS₃/rGO int and a-MoS₃/rGO 250 samples, which substantially increased as the annealing temperature was raised. As a fact, these two peaks were sensitive to the laser exposure and increased as the laser power or exposure time was raised, due to the localized laser heating as reported in literature [50]. This indicates that the formation of c-MoS2 is negligible during the microwave reduction step and at 250 °C thermal annealing, consistent with the XRD results. The composition may be dominated by a-MoS₃ in these two samples and thus they are denoted as a-MoS₃/rGO int and a-MoS₃/rGO 250. It is worth noting that the intensity of MoS $_2$ $(E^1_{2g} \mbox{ and } A_{1g})$ to rGO (D and G band) peaks increased with increasing annealing temperature, ascertaining the presence of higher composition of MoS2 in samples annealed at higher temperatures, owing to conversion of a-MoS3 to c-MoS2. Quantitatively, the ratio of intensity of A_{1g} to D band increases from 0.38 for a-MoS₃/rGO int to 2.97 for c-MoS₂/rGO 600. This trend agrees well with the evolution of crystalline 2H MoS2 diffraction peaks when increasing the annealing temperatures in XRD (Fig. 1(a)). On the other hand, the characteristic Raman vibrations observed in the a-MoS_x polymeric clusters prepared by electrodeposition, such as ν(Mo-S)_{coupled} at 320 cm⁻¹, ν (S_{apical}–Mo) at 445 cm⁻¹, ν (S–S)_{terminal} at 520 cm⁻¹ and ν (S–S)_{bridging} at 550 cm⁻¹ [29], were not observed in any of our MoS_x/rGO hybrids. Clearly, the structure of a-MoS₃ deposited on rGO in this work is different from the polymeric clusters prepared by electrodeposition or other wet chemical syntheses reported in literature [14,16, 29,31]. Instead, our materials can be well explained based on 1D chain-like a-MoS₃ structures based on Weber's and Hibble's models, as supported by the XPS results in the next section.

3.2. Materials composition estimation

XPS analysis was carried out to understand the chemical composition of the MoS_x/rGO hybrids. Fig. 3(a) shows that the Mo 3d spectrum of a-MoS₃/rGO int can be deconvoluted into three Mo $3d_{5/2}$ and Mo $3d_{3/2}$

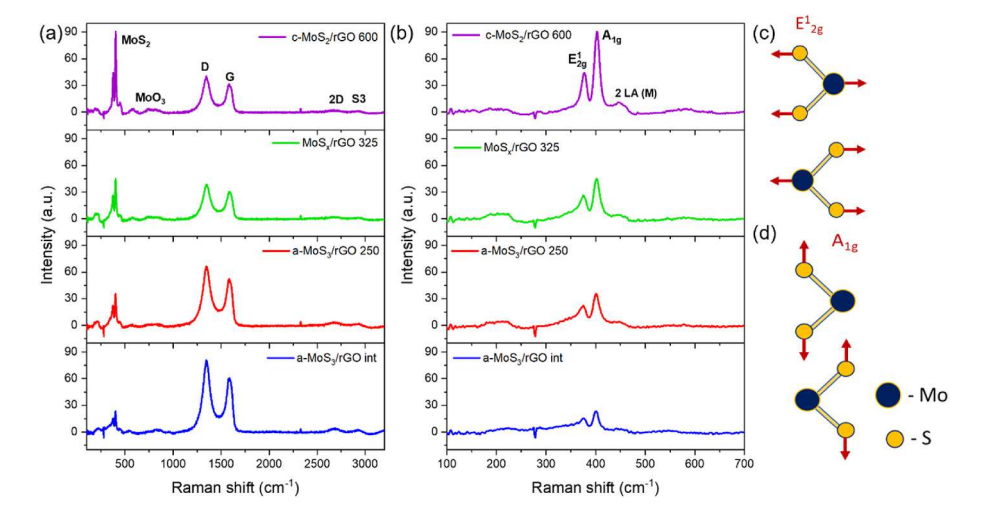


Fig. 2. Comparison of Raman spectra of a-MoS₃/rGO int, a-MoS₃/rGO 250, MoS_x/rGO 325 and c-MoS₂/rGO 600: (a) from 100 to 3200 cm⁻¹, and (b) from 100 to 700 cm⁻¹. Schematic representation of (c) E_{2g}^1 in-plane vibration and (d) A_{1g} out-of-plane vibration of MoS₂.

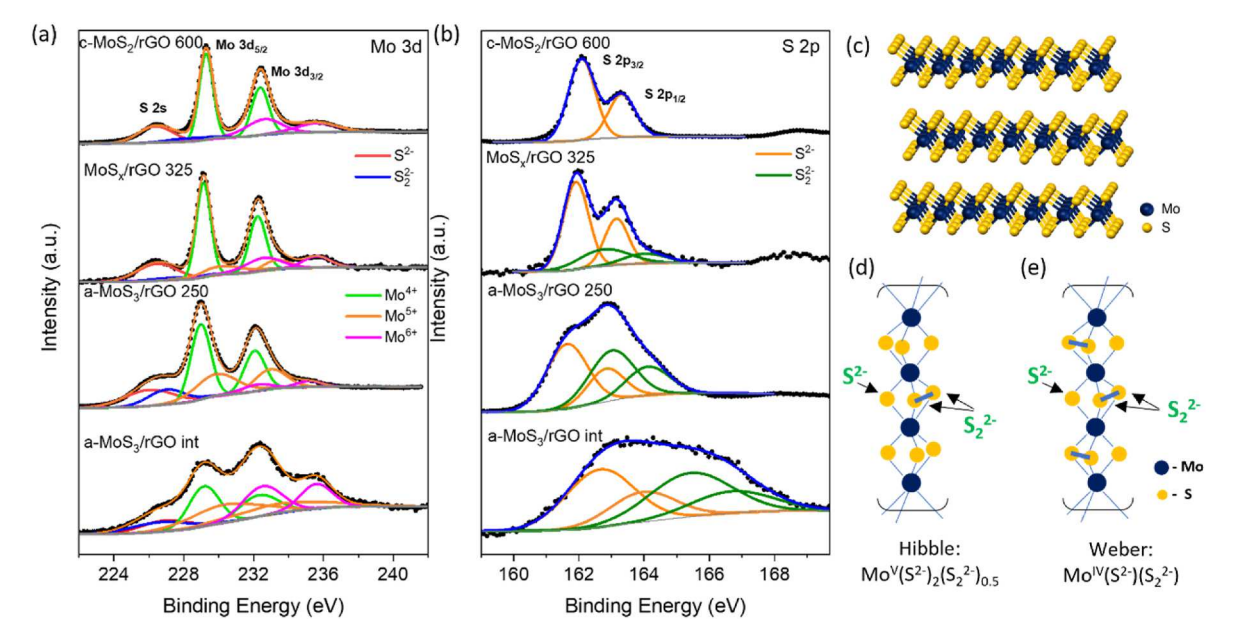


Fig. 3. High-resolution XPS spectra of (a) Mo 3d and (b) S 2p of a-MoS₃/rGO int, a-MoS₃/rGO 250, MoS_x/rGO 325 and c-MoS₂/rGO 600. (c) Schematic drawing of the two-dimensional crystal structure of 2H MoS₂. (d) Schematic drawing of Hibble model of the 1D MoS₃ chain structure with S_2^{2-} bond in every other S₃ links, resulting in the formula $Mo^{V}(S^{2-})_2(S_2^{2-})_{0.5}$. (e) Schematic drawing of Weber model of the 1D MoS₃ chain structure with S_2^{2-} in every S₃ link with the formula $Mo^{IV}(S^{2-})(S_2^{2-})$.

doublets positioned at the binding energy (BE) of 229.16 and 232.26 eV, 230.41 and 233.51 eV, and 232.49 and 235.59 eV, respectively, corresponding to Mo^{IV}, Mo^V and Mo^{VI} from MoS₃ and unreacted ATM precursors [35,51]. It is worth noting that the shape and BE of raw Mo 3d spectrum of a-MoS₃/rGO int are quite different from the annealed MoS_x/rGO hybrids, likely due to incomplete conversion of ATM precursors into MoS₃. The S 2p spectrum of a-MoS₃/rGO int was deconvoluted into two pairs of doublets (2p $_{3/2}$ and 2p $_{1/2}$), one pair at lower BE of 162.65 and 163.96 eV and the other pair at higher BE of 165.42 and 166.69 eV, as shown in Fig. 3(b). The doublet at the lower BE can be attributed to the S^{2-} of MoS_3 (orange curves) while the higher BE doublet (green curves) to the S_2^{2-} of MoS₃ [35,51]. There was about 52.4% of S atoms present in form of S^{2-} and ~47.6% in form of S_{2}^{2-} , giving an atomic ratio in these two forms (S_2^{2-}/S^{2-}) of 0.91:1 in a-MoS₃/rGO int. It is to be noted that Mo 3d spectra has a shoulder peak at around 226 eV attributed to the singlet peak of S 2s. Like the S 2p spectra, the S 2s spectra were fitted with two peaks corresponding to S² and S_2^{2-} ligands in MoS₃.

The XPS spectra of the three thermal annealed MoS_x/rGO hybrids were analyzed by the same methods. The BE and relative atomic percentage (at%) of Mo and S species at different valence states of all four MoS_x/rGO hybrids are listed in Table S1 and presented in Fig. S2. Clearly, as the annealing temperature is raised, the at% of Mo^{IV} steadily increases from 33.3% to 79.6% (Fig. S2(a)) while that of Mo^V decreases from \sim 36% to 0% (Fig. S2(b)). It is not surprising that more Mo^{V} and Mo^{VI} are reduced to Mo^{IV} in the reducing atomosphere (i.e., 3% $H_2/97\%$ Ar) when heated to higher temperatures. However, the at% of Mo^{VI} was more complicated, first decreased to 8.2% (in a-MoS₃/rGO 250) and then increased to 22.9% (in MoSx/rGO 325) and 20.4% (in c-MoS₃/rGO 600). This might be due to the presence of unreacted (NH₄)₂MoS₄ precursors in a-MoS₃/rGO int and formation of MoO₃ (by reacting with oxygenated groups in rGO) at elevated annealing temperature of 325 °C and 600 °C. The relative at% of S^{2-} among all S atoms monotonically increased from 52.4% to 100% while that of S_2^{2-} monotonically decreased from 47.6% to 0% as the annealing temperature was raised. In c-MoS₂/rGO 600, all MoS_x presents as pure c-MoS₂ except those forming MoO₃, which is consistent with the clear XRD and SAED patterns. The overall atomic ratio of S to Mo derived by XPS analyses are shown in

Fig. S3(a), which monotonically decreases from 3.6 (in a-MoS $_3$ /rGO int) to 2.2 (in a-MoS $_3$ /rGO 600). These values agree well with the results by CHNS elemental analysis shown in Fig. S3(b).

As shown above, the composition and structure of MoS_v/rGO hybrids show a clear trend correlated with the preparation conditions, which provides a unique capability to tune key parameters for investigation of their effects on the HER catalytic activity. However, the materials composition is rather complicated and the lack of characteristic features of a-MoS₃ makes it even more difficult. To simplify the problems so that the key information can be extracted, we derive the estimated materials composition based on stoichiometric models illustrated below. Firstly, starting from the intermediate materials (i.e., a-MoS₃/rGO int), the presence of both Mo^{IV} (33.3%) and Mo^V (35.1%) states reveals that a-MoS₃/rGO int consists of a mixture of 1D chain-like a-MoS₃ structures proposed by Hibble (Fig. 3(d)) and Weber (Fig. 3(e)). We attribute all Mo^V species to Hibble-type a-MoS₃ structure with the formula $Mo^{V}(S^{2-})_{2}(S_{2}^{2-})_{0.5}$, all Mo^{IV} species to Weber-type a-MoS₃ structure with the formula $Mo^{IV}(S^{2-})(S_2^{2-})$, and all Mo^{VI} species to ATM residues. No c-MoS₂ is formed at this condition (as supported by XRD, SAED and Raman spectra). From the relative at% of Mo^{IV}, Mo^V, S₂²⁻ and S²⁻ (Fig. S2 and Table S1), the composition of a-MoS₃/rGO int can be estimated to consist of \sim 35% of Mo^V(S²⁻)₂(S²⁻)_{0.5} (Hibble a-MoS₃), \sim 33% of $Mo^{IV}(S^{2-})(S_2^{2-})$ (Weber a-MoS₃) and ~32% Mo^{VI} from unreacted ATM precursors, as shown in Table 1.

When the sample was annealed at 250 °C, we can assign the composition according to the relative at% of Mo^{IV} and Mo^V similar as above. The increase in Mo^{IV} content (from 33% to 55%) can be attributed to formation of more Weber-type a-MoS₃ (i.e., Mo^{IV}(S²⁻)(S²⁻₂)) while the content of Hibble-type a-MoS₃ (i.e., Mo^V(S²⁻)₂(S²⁻₂)_{0.5}) remained about the same (37%). The Mo^{VI} content was substantially reduced from 32% to only 8%, indicating further conversion of ATM precursor to a-MoS₃ while the c-MoS₂ content was still negligible. Considering the higher temperature, the Mo^{VI} (8%) is likely in form of MoO₃ due to reaction with oxygen species in GO and rGO.

Raising the annealing temperature further to 325 $^{\circ}$ C clearly reduced some Mo^V to Mo^{IV} and converted a large portion of a-MoS₃ into c-MoS₂. The formation of c-MoS₂ is reflected by the emergence of weak 2H MoS₂ XRD peaks in the MoS₂/rGO 325 sample. As discussed above, the higher

Table 1
The composition and stoichiometric formula of different MoS_x/rGO hybrids.

	Stoichiometric formula	a-MoS ₃ /rGO int	a-MoS $_3$ /rGO 250	$MoS_x/rGO~325$	c-MoS ₂ /rGO 600
Mo ^{IV}	a-MoS ₃ (Weber): $Mo^{IV}(S^{2-})(S_2^{2-})$	33%	55%	18%	_
	c-MoS ₂ : $Mo^{IV}(S^{2-})_2$	_	_	43%	80%
Mo^{V}	a-MoS ₃ (Hibble): $Mo^{V}(S^{2-})_{2}(S_{2}^{2-})_{0.5}$	35%	37%	16%	_
Mo^{VI}	$(NH_4)_2MoS_4$ or MoO_3	32% (NH ₄) ₂ MoS ₄	8% MoO ₃	$23\% \text{ MoO}_3$	$20\% \text{ MoO}_3$
Atomic ratio of total Mo: S (calculated by the composition in rows 2-5)		1:3.3	1:2.8	1:2.2	1:1.6
Atomic ratio of total Mo : S (by XPS)		1:3.6	1:3.0	1:2.3	1:2.2
Atomic ratio of S in S_2^{2-} : S_2^{2-} (calculated by the composition in rows 2–5)		0.44:1	0.62:1	0.38:1	0:1
Atomic ratio of S in S_2^2 : S^2 (by XPS)		0.91 : 1 ^a	0.81:1	0.38:1	0:1

^a The BEs of S 2p peaks of S² species in (NH₄)₂MoS₄ precursor are upshift and overlapped with the S²₂ peaks of a-MoS₃ (see Fig. 3(b)), thus they tended to be miscounted as S²₂ species in curve fitting.

annealing temperature had a side effect to form more MoO₃ (i.e., 23% accounting for Mo^{VI} comparing to 8% in a-MoS₃/rGO 250). The stoichiometric composition of MoS₂/rGO 325 is much more complicated due to the fact that Mo^{IV} may consist of both Weber-type a-MoS₃ (i.e., Mo^{IV}(S²⁻)(S²⁻₂)) and c-Mo^{IV}S₂. However, the composition of each form can still be estimated by considering the two facts derived from XPS measurements, i.e., the relative at% of Mo species at valence states of Mo^{IV}, Mo^V and Mo^{VI} and the relative at% of S species in form of S²⁻ and S²⁻₂, as described in the SI. With this method, it was estimated that the MoS₂/rGO 325 sample consisted of ~18% of Mo^{IV}(S²⁻)(S²⁻₂) (Weber a-MoS₃), ~16% of Mo^V(S²⁻)₂(S²⁻₂)_{0.5} (Hibble a-MoS₃), ~43% of c-Mo^{IV}S₂ and ~23% Mo^{VI}O₃. Due to the presence of a mixture of a-MoS₃ and c-MoS₂, we denote this sample as MoS_x/rGO 325 to distinguish it from a-MoS₃ (in intermediate form and annealed at 250 °C) and c-MoS₂ (at 600 °C).

At 600 °C, all a-MoS $_3$ was converted into c-MoS $_2$ while a small amount of MoO $_3$ (\sim 20%) was retained. It is notable that the small amount of MoO $_3$ in the hybrid materials has a finite solubility in water (\sim 1.4 g/L at room temperature) and can be completely dissolved before running HER measurements, as reported in an operando Raman studies [29,52]. Thus, the MoO $_3$ content does not affect the electrocatalysis results.

The estimated compositions based on the aforementioned methods are validated by comparing the calculated atomic ratio with the XPS data. The 6th row in Table 1 shows the atomic ratios of Mo to S based on the stoichiometric calculation of the listed compositions, which are 1:3.3, 1:28, 1:2.2 and 1:16 for the four samples. While these numbers are a little bit off from those derived from XPS analysis (i.e., 1:3.6, 1:3.0, 1:2.3 and 1:2.2), they followed the exact trend. Similarly, the atomic ratio of S in form of S_2^{-} to S_2^{-} by the stoichiometric calculation (the 2nd row from bottom in Table 1) follows the same trend as those derived from XPS analysis (the bottom row in Table 1) except the a-MoS₃/rGO int sample. Interestingly, despite the S species in ATM precursor (NH₄)₂MoS₄ is in S_2^{-} form, its BE upshift from that of MoS₂ by > 1.5 eV and is convoluted with the S_2^{-} form. This explained the abnormal higher atomic ratio of S_2^{-} to S_2^{-} in a-MoS₃/rGO int.

3.3. Electrocatalytic activity of MoSx/rGO hybrid

Electrochemical characterization of the MoS_x/rGO hybrids were conducted to evaluate their electrocatalytic activity for HER. The catalyst loading was maintained as $125~\mu g/cm^2$ for all catalysts in this work. The HER performance of precious metal catalyst Pt/C JM ($20~\mu g/cm^2$) was collected for comparison. The commercial Pt/C JM catalyst showed an overpotential of 40 mV at $10~mA/cm^2$ for HER. From the LSV curves shown in Fig. 4(a), it was found that, among all the MoS_x/rGO hybrid catalysts, a- MoS_3/rGO 250 exhibited the lowest overpotential of 208.2 mV for HER at $10~mA/cm^2$ current density, indicating its high catalytic activity. The enhanced activity of a- MoS_3 agrees with literature and can be attributed to the abundant exposed active sites [12,14]. The c- MoS_2/rGO 600 exhibited the lowest electrocatalytic activity for HER among MoS_x/rGO hybrids, with an overpotential of 433.6 mV at 10

mA/cm². However, when compared to commercial bulk crystalline 2H MoS₂ (575.8 mV HER overpotential at 10 mA/cm²), c-MoS₂/rGO 600 showed enhanced electrocatalytic activity due to the nanopatch morphology that provides more exposed active edge sites. The a-MoS₃/rGO int and MoS₂/rGO 325 showed HER overpotentials of 221 and 293.4 mV, respectively, at 10 mA/cm². Interestingly, the order of increasing Mo^V deduced from XPS is in the same order as the increasing HER activity with c-MoS $_2$ /rGO 600 < MoS $_x$ /rGO 325 < a-MoS $_3$ /rGO int < a-MoS₃/rGO 250. It is to be noted that all the presented LSV curves are subject to iR-correction. Fig. S4(a) shows the LSV curves before and after iR correction for all catalysts, which only have a small difference. Fig. S4 (b) shows the EIS spectra of all the catalysts, which were fitted to a Randles equivalent circuit to find the uncompensated solution resistance to perform iR correction to the LSV curves. Experimental section provides details on the iR correction procedure. Fig. S5 (a) shows the LSV curves of all electrocatalysts exceeding 90 mA/cm² of HER current density. Fig. S5 (b) shows that rotating the electrode at 1600 rpm helps to accelerate the H2 gas diffusion from the electrode to the bulk solution and reduce the noise of the LSV curve at the high current density region (>60 mA/cm²). But it has little effects in the low current density region $(<60 \text{ mA/cm}^2).$

Further, Tafel analysis was done for LSV curves of MoS_x/rGO hybrid catalysts, as shown in Fig. 4(b), to identify the rate-determining step for HER. The best performing MoS_x/rGO catalyst, i.e., a- MoS_3/rGO 250, showed the lowest Tafel slope of 52.8 mV/decade, revealing that HER follows Volmer-Heyrovsky pathway agreeing with previous reports [29, 30]. The a- MoS_3/rGO int was found to have a little bit higher Tafel slope of 58.3 mv/decade, followed by MoS_2/rGO 325 (91.5 mV/decade) and c- MoS_2/rGO 600 (128.7 mV/decade). The order is consistent with the increasing order of the overpotential value at 10 mA/cm².

For further evaluation, the relative value of HER turnover frequency (TOF) was calculated to determine the intrinsic catalytic activity of the MoS_x/rGO hybrids. We followed an estimation process proposed by Jaramillo and co-workers that are detailed in the SI [16]. It was calculated using the equation [53,54] given below:

$$TOF\left(s^{-1}\right) = \frac{j \, x N_A}{n \, x \, F \, x \, \Gamma} \tag{7}$$

where j is the current density (mA/cm²) at the HER overpotential of 208 mV where the best MoS_x/rGO catalyst a-MoS₃/rGO 250 provides 10 mA/cm² HER current density (see details in SI), N_A is the Avogadro constant, F is the Faraday constant, n is the number of electrons transferred to generate one molecule of H_2 , and Γ is the surface concentration of electrocatalytic active sites. To make a consistent comparison, all a-MoS_x/rGO catalysts are treated as MoS_2 analogues. The Γ value of MoS_2 analogues is calculated by the equation:

$$\Gamma = N_{MoS2} \times ECSA \tag{8}$$

where N_{MoS2} is the number of MoS_2 units/cm² which is equal to $1.164 \times 10^{15} \, MoS_2/cm^2$ and ECSA is the electrocatalytic active surface area [53, 54]. The ECSA of MoS_x/rGO materials is measured by dividing the

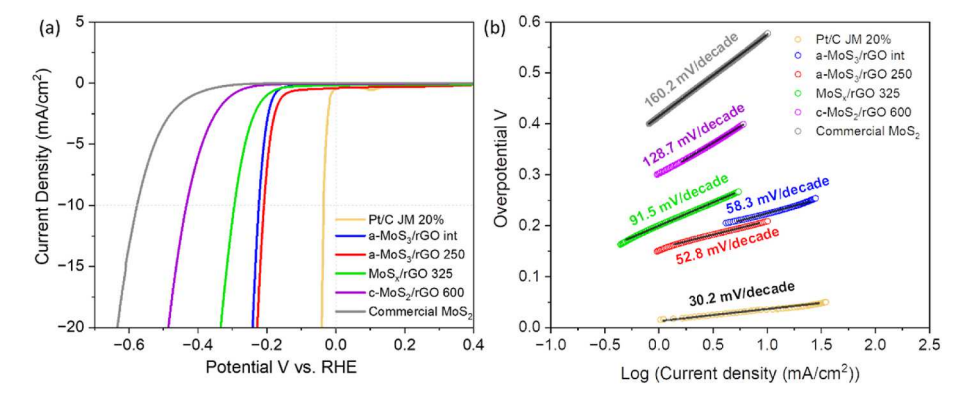


Fig. 4. Electrochemical LSV HER studies in 0.50 M H_2SO_4 . (a) LSV polarization curves and (b) corresponding Tafel plots of commercial Pt/C JM 20 % (yellow), a-MoS₃/rGO int (blue), a-MoS₃/rGO 250 (red), MoS_x/rGO 325 (green), c-MoS₂/rGO 600 (purple) and commercial MoS₂ (grey). (For interpretation of the references to colour in this figure legend, the reader is referred to the Web version of this article.)

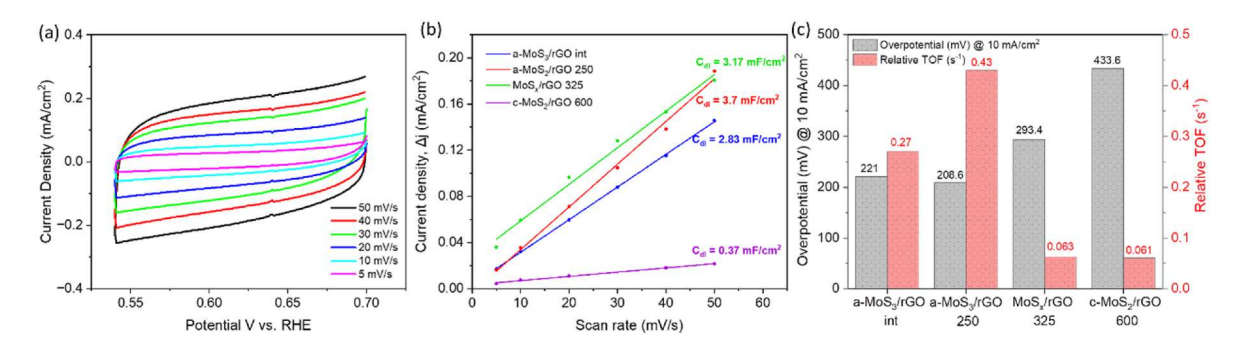


Fig. 5. Determination of the relative value of HER TOF. (a) Cyclic voltammogram of a-MoS $_3$ /rGO 250 collected at different scan rates in the non-faradic region to measure the capacitive current from charging/discharging the electrical double layer. (b) Linear fitting of the capacitive currents of catalysts vs. scan rates to determine the electrical double-layer capacitance values for a-MoS $_3$ /rGO int, a-MoS $_3$ /rGO 250, MoS $_x$ /rGO 325 and c-MoS $_2$ /rGO 600 electrocatalysts. (c) Comparison of overpotential at 10 mA/cm 2 and the relative TOF values at 208 mV overpotential for a-MoS $_3$ /rGO int, a-MoS $_3$ /rGO 250, MoS $_x$ /rGO 325 and c-MoS $_2$ /rGO 600 electrocatalysts.

non-faradaic electrical double-layer capacitance($C_{\rm dl}$) associated with charging/discharging of the specific MoS_x/rGO catalyst. The specific capacitance is 60 μ F/cm² for a flat monolayer MoS₂ standard.

Fig. 5(a) and Fig. S6 show the CV in the non-faradaic potential region conducted at different scan rates for the MoS_x/rGO hybrids. The difference in anodic and cathodic current density at the center of the CV curves (Δ j) versus the scan rate is plotted in Fig. 5(b). The data from all four MoS_x/rGO catalysts showed linear curves, validating the pure capacitive behavior. The magnitude of C_{dl} was calculated from the slope as: 2.83 mF/cm² for a-MoS₃/rGO int, 3.7 mF/cm² for a-MoS₃/rGO 250, 3.17 mF/cm² for MoS_2/rGO 325 and 0.37 mF/cm² for c-MoS₂/rGO 600. The high C_{dl} of a-MoS₃/rGO 250 indicates that it has the highest density

of exposed electrochemical active sites. Corresponding to this, the TOF of a-MoS $_3$ /rGO 250 was calculated to be 0.43 H $_2$ /s per site at 208 mV overpotential (for 10 mA/cm 2). The TOF values of a-MoS $_3$ /rGO int, MoS $_2$ /rGO 325 and c-MoS $_2$ /rGO 600 were found to be 0.27 H $_2$ /s, 0.063 H $_2$ /s and 0.061 H $_2$ /s per site, respectively, at the same overpotential (i. e., 208 mV). The HER overpotential and TOF values are listed in Table S2 and presented in Fig. 5(c), which provides a consistent view of the HER catalytic activity of these catalysts. Overall, a-MoS $_3$ /rGO 250 showed the highest intrinsic catalytic activity for HER among all MoS $_x$ /rGO hybrids studied in this work.

Table S3 shows the comparison of HER activity in this study with 10 related studies in literature. The a-MoS₃/rGO 250 exhibits a competitive

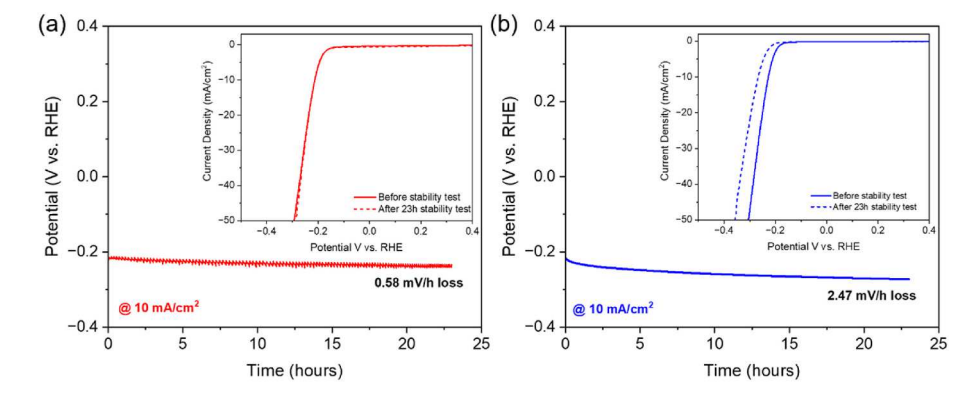


Fig. 6. (a) Electrode stability test of a-MoS₃/rGO 250 at 10 mA/cm² over 23 h with the inset showing the polarization curves before and after the stability test. (b) Electrode stability test of a-MoS₃/rGO int at 10 mA/cm² over 23 h with inset showing the polarization curves before and after the stability test.

HER activity overpotential at 10 mA/cm² with high TOF values for lower catalyst loading when compared to current reports. In future studies, high surface area graphitic carbon supports can be utilized to maximize the ${\rm MoS}_{\rm x}$ dispersion and morphology so that the HER catalytic activity can be further improved.

Finally, the durability tests were conducted using chronopotentiometry with the top two catalysts, i.e., a-MoS₃/rGO 250 and a-MoS₃/rGO int for a period of 23 h at 10 mA/cm² as shown in Fig. 6. The a-MoS₃/rGO 250 showed excellent stability with the HER overpotential increase at the rate of only 0.58 mV/h during the durability test. Whereas the HER overpotential increased much faster at a rate of 2.47 mV/h for the a-MoS₃/rGO int. In addition, an LSV was performed after the completion of durability test to evaluate the change in their electrocatalytic activities. The change in overpotential with a-MoS₃/rGO 250 hybrid was negligible, indicating that the active sites on a-MoS₃/ rGO 250 remain stable after continuously operating for long durations. However, for a-MoS $_3$ /rGO int, the HER overpotential increased by \sim 37 mV after the long-term durability test, indicating the instability of the active sites during continuous operation. The better stability and higher activity of a-MoS₃/rGO 250 over MoS₃/rGO int can be attributed to the stable and active Weber-type a-MoS₃ structure, i.e., $Mo^{IV}(S^{2-})(S_2^{2-})$, aided by the additional annealing step at 250 °C in 3% H₂/97% Ar.

3.4. Insights on the catalytic active sites

It is important to uncover the catalytic active sites that are responsible for the high intrinsic catalytic activity of a-MoS $_3$ /rGO 250 to design and develop better HER electrocatalysts in the future. By correlating chemical compositions derived from XPS with the electrocatalytic activity, it was found that the composition of a-MoS $_3$ (in form of both Hibble-type and Weber-type) was the highest in a-MoS $_3$ /rGO 250 which exhibits the highest HER activity among all the hybrid catalysts. When the composition of a-MoS $_3$ decreased in the order of a-MoS $_3$ /rGO int, MoS $_2$ /rGO 325, and c-MoS $_2$ /rGO 600, the electrocatalytic activity for HER decreased as well.

On the other hand, while closely examining the HER polarization curve shown in Fig. 4(a), a small reduction current over a broad region from 0.4~V to -0.1~V vs. RHE was observed before onset of significant HER for all MoS_x/rGO hybrid catalysts (as enlarged in Fig. S7). A similar reduction process was observed by Hu et al. and was attributed to the electroreduction of S_2^{2-} to S^{2-} [12]. It is to be noted that the LSV curves shown in Fig. 4(a) were collected after CV activation for 50 cycles. For comparison, LSV curves were also collected prior to activation. Interestingly, as shown in Fig. S8(a), two reduction peaks were observed at $0.050\ V$ and $-0.086\ V$ vs. RHE for a-MoS $_3/rGO$ int and a-MoS $_3/rGO\ 250$ hybrids in the LSV curves collected from the fresh electrodes. The fresh LSVs of these two catalysts almost overlapped with each other. In contrast, these two peaks are much weaker in MoS2/rGO 325 and c-MoS₂/rGO 600, accompanying a much lower capacitive baseline current consistent with CVs in the non-faradaic region (Fig. S8(b)). With CV activation, the magnitude of these initial reduction peaks in a-MoS₃/rGO int and a-MoS₃/rGO 250 decreased significantly to form the small broad reduction region as shown in Figs. S9(a) and S9(b). But, after CV activation, the electrocatalytic activity of a-MoS₃/rGO 250 showed a reduction in HER overpotential by 13 mV at 10 mA/cm² (Fig. S9(b)), while a-MoS₃/rGO int did not show such a change. The boost in activity of a-MoS₃/rGO 250 with CV activation cycles indicates creation of new HER active sites. As reduction of S_2^{2-} to S_2^{2-} is found to occur during the activation, it is likely that these sulfur ligands may contribute to the improvement in HER activity. Similar observations were reported by Hu et al. [12,30] and Yeo et al. [12,30]. On the other hand, enhanced HER activity by the defect density of Mo^V were reported by Li et al. [31,35] and Tran et al. [31,35]. Both a-MoS $_3$ /rGO 250 and a-MoS $_{\!3}/rGO$ int in our study have a high Mo^{V} content. From these perspectives, it is likely that both Mo^V and sulfur ligands play the catalytic role in the HER activity of a-MoS₃.

4. Conclusion

A controllable microwave-assisted synthesis was used to prepare amorphous MoS₃ (a-MoS₃) on a rGO template as HER electrocatalysts. By thermal annealing of the microwave-synthesized a-MoS₃/rGO intermediate material at various temperatures, a family of MoS_x/rGO hybrids from a-MoS₃ to c-MoS₂ were produced. From Raman spectroscopy and XPS analyses, these materials appeared to have very different structure from the chained polymeric clusters that were synthesized by electrodeposition or other wet chemical processes. The major compositions of the microwave-synthesized intermediate (a-MoS₃/rGO int) and the one annealed at 250 $^{\circ}$ C (a-MoS₃/rGO 250) can be described by a mixture of two types of a-MoS₃, i.e., Hibble-type $Mo^{V}(S^{2-})_{2}(S_{2}^{2-})_{0.5}$ and Weber-type Mo^{1V} (S^{2-}) (S^{2-}). When a higher annealing temperature, such as 325 °C, is applied, the a-MoS₃ starts to be converted into crystalline MoS₂ hybrids and forms pure c-MoS₂/rGO at 600 °C. The a-MoS₃/ rGO 250 exhibited the highest HER catalytic activity with an overpotential of 208 mV at 10 mA/cm², a low Tafel slope of 52 mV/decade, a high double layer capacitance of 3.7 mF/cm² and a high relative TOF value of 0.43 H₂/s per site at the HER overpotential of 208 mV. The enhanced catalytic activity can be attributed to the catalytic role of both Mo^V and sulfur ligands of the a-MoS₃/rGO 250. It illustrates the importance of defect engineering in optimizing the HER catalytic activity of MoSx catalysts. This study demonstrated a rapid and controllable synthesis method to prepare a family of a-MoS₃/rGO and c-MoS₂/ rGO hybrids for HER electrocatalysis.

CRediT authorship contribution statement

Archana Sekar: Conceptualization, Formal analysis, Investigation, Methodology, Validation, Visualization, Writing - original draft. Kamalambika Muthukumar: Methodology, Formal analysis, Investigation. Sabari Rajendran: Formal analysis, Investigation, Methodology, Writing - review & editing. Jun Li: Conceptualization, Formal analysis, Funding acquisition, Methodology, Validation, Project administration, Resources, Supervision, Writing - review & editing.

Declaration of competing interest

The authors declare that they have no known competing financial interests or personal relationships that could have appeared to influence the work reported in this paper.

Acknowledgement

This work was supported by the National Science Foundation grants DMR-1707585 and CBET-2054754. We would like to thank Dr. Dan Boyle at Kansas State University's microscopy facility for help in TEM measurements and Prof. Christer Aakeroy at Kansas State University for support in TGA measurements. We wish to thank Dr. Sarah Cady at Iowa State University's Chemical Instrumentation Facility for assistance pertaining to the PE 2100 CHN/S elemental analysis in this study. The XPS characterization was performed in the Nebraska Nanoscale Facility: National Nanotechnology Coordinated Infrastructure and the Nebraska Center for Materials and Nanoscience, which are supported by the National Science Foundation under Award ECCS: 2025298 and the Nebraska Research Initiative.

Appendix A. Supplementary data

Supplementary data to this article can be found online at https://doi.org/10.1016/j.ijhydene.2023.11.107.

References

- [1] Shiva Kumar S, Himabindu V. Hydrogen production by PEM water electrolysis a review. Mater Sci Energy Technol 2019;2:442–54.
- [2] Chatterjee S, Parsapur RK, Huang K-W. Limitations of ammonia as a hydrogen energy carrier for the transportation sector. ACS Energy Lett 2021;6:4390–4.
- [3] Idriss H. Hydrogen production from water: past and present. Curr Opin Chem Eng 2020;29:74–82.
- [4] Guha A, Veettil Vineesh T, Sekar A, Narayanaru S, Sahoo M, Nayak S, Chakraborty S, Narayanan TN. Mechanistic insight into enhanced hydrogen evolution reaction activity of ultrathin hexagonal boron nitride-modified Pt electrodes. ACS Catal 2018:8:6636-44.
- [5] Lim T, Kim S-K. Non-precious hydrogen evolution reaction catalysts: stepping forward to practical polymer electrolyte membrane-based zero-gap water electrolyzers. Chem Eng J 2022;433:133681.
- [6] Pivovar BS, Ruth MF, Myers DJ, Dinh HN. Hydrogen: targeting \$1/kg in 1 decade. Electrochem Soc Interface 2021;30:61.
- [7] Guo Y, Park T, Yi JW, Henzie J, Kim J, Wang Z, Jiang B, Bando Y, Sugahara Y, Tang J, Yamauchi Y. Nanoarchitectonics for transition-metal-sulfide-based electrocatalysts for water splitting. Adv Mater 2019;31:1807134.
- [8] Yap FM, Loh JY, Ong W-J. Synergistic integration of self-supported 1T/2H-WS₂ and nitrogen-doped rGO on carbon cloth for pH-universal electrocatalytic hydrogen evolution. Nano Research: 2023.
- [9] Voiry D, Yang J, Chhowalla M. Recent strategies for improving the catalytic activity of 2D TMD nanosheets toward the hydrogen evolution reaction. Adv Mater 2016;28:6197–206.
- [10] Yang C, Li X, Liang Y. Recent advances in molybdenum diselenide-based electrocatalysts: preparation and application in the hydrogen evolution reaction. Inorg Chem Front 2023;10:5517–54.
- [11] Yang H, Zhang P, Zheng Q, Ali T, Raza S. Vacancy engineering in tungsten induced electronic structure optimization of MoSe₂ for enhanced electrocatalytic hydrogen evolution reaction. Int J Hydrogen Energy 2023;48:35433–42.
- [12] Merki D, Fierro S, Vrubel H, Hu X. Amorphous molybdenum sulfide films as catalysts for electrochemical hydrogen production in water. Chem Sci 2011;2: 1262–7
- [13] Jaramillo TF, Jørgensen KP, Bonde J, Nielsen JH, Horch S, Chorkendorff I. Identification of active edge sites for electrochemical H₂ evolution from MoS₂ nanocatalysts. Science 2007;317:100–2.
- [14] Wang D, Li H, Du N, Hou W. Amorphous molybdenum sulfide monolayer nanosheets for highly efficient electrocatalytic hydrogen evolution. Chem Eng J 2020;398:125685.
- [15] Hinnemann B, Moses PG, Bonde J, Jørgensen KP, Nielsen JH, Horch S, Chorkendorff I, Nørskov JK. Biomimetic hydrogen evolution: MoS₂ nanoparticles as catalyst for hydrogen evolution. J Am Chem Soc 2005;127:5308–9.
- [16] Benck JD, Chen Z, Kuritzky LY, Forman AJ, Jaramillo TF. Amorphous molybdenum sulfide catalysts for electrochemical hydrogen production: insights into the origin of their catalytic activity. ACS Catal 2012;2:1916–23.
- [17] Wang F, Shifa TA, Zhan X, Huang Y, Liu K, Cheng Z, Jiang C, He J. Recent advances in transition-metal dichalcogenide based nanomaterials for water splitting. Nanoscale 2015;7:19764–88.
- [18] Xie S, Sun B, Sun H, Zhan K, Zhao B, Yan Y, Xia BY. Engineering of molybdenum sulfide nanostructures towards efficient electrocatalytic hydrogen evolution. Int J Hydrogen Energy 2019;44:15009–16.
- [19] Gopalakrishnan D, Damien D, Shaijumon MM. MoS₂ quantum dot-interspersed exfoliated MoS₂ nanosheets. ACS Nano 2014;8:5297–303.
- [20] Li H, Tsai C, Koh AL, Cai L, Contryman AW, Fragapane AH, Zhao J, Han HS, Manoharan HC, Abild-Pedersen F, Nørskov JK, Zheng X. Activating and optimizing MoS₂ basal planes for hydrogen evolution through the formation of strained sulphur vacancies. Nat Mater 2016;15:48–53.
- [21] Lukowski MA, Daniel AS, Meng F, Forticaux A, Li L, Jin S. Enhanced hydrogen evolution catalysis from chemically exfoliated metallic MoS₂ nanosheets. J Am Chem Soc 2013;135:10274–7.
- [22] Chen Z, Cummins D, Reinecke BN, Clark E, Sunkara MK, Jaramillo TF. Core–shell MoO₃–MoS₂ nanowires for hydrogen evolution: a functional design for electrocatalytic materials. Nano Lett 2011;11:4168–75.
- [23] Kong D, Wang H, Cha JJ, Pasta M, Koski KJ, Yao J, Cui Y. Synthesis of MoS₂ and MoSe₂ Films with Vertically Aligned Layers. Nano Lett 2013;13:1341–7.
- [24] Kibsgaard J, Chen Z, Reinecke BN, Jaramillo TF. Engineering the surface structure of MoS₂ to preferentially expose active edge sites for electrocatalysis. Nat Mater 2012;11:963–9.
- [25] Liang KS, Cramer SP, Johnston DC, Chang CH, Jacobson AJ, deNeufville JP, Chianelli RR. Amorphous MoS₃ and WS₃. J Non-Cryst Solids 1980;42:345–56
- [26] Weber T, Muijsers JC, Niemantsverdriet JW. Structure of amorphous MoS₃. J Phys Chem 1995;99:9194–200.
- [27] Hibble SJ, Wood GB. Modeling the structure of amorphous MoS₃: a neutron diffraction and reverse Monte Carlo study. J Am Chem Soc 2004;126:959–65.
- [28] Lassalle-Kaiser B, Merki D, Vrubel H, Gul S, Yachandra VK, Hu X, Yano J. Evidence from in situ X-ray absorption spectroscopy for the involvement of terminal disulfide in the reduction of protons by an amorphous molybdenum sulfide electrocatalyst. J Am Chem Soc 2015;137:314–21.
- [29] Deng Y, Ting LRL, Neo PHL, Zhang Y-J, Peterson AA, Yeo BS. Operando Raman spectroscopy of amorphous molybdenum sulfide (MoS_x) during the

- electrochemical hydrogen evolution reaction: identification of sulfur atoms as catalytically active sites for $\rm H^+$ reduction. ACS Catal 2016;6:7790–8.
- [30] Ting LRL, Deng Y, Ma L, Zhang Y-J, Peterson AA, Yeo BS. Catalytic activities of sulfur atoms in amorphous molybdenum sulfide for the electrochemical hydrogen evolution reaction. ACS Catal 2016;6:861–7.
- [31] Tran PD, Tran Thu V, Orio M, Torelli S, Truong QD, Nayuki K, Sasaki Y, Chiam Sing Y, Yi R, Honma I, Barber J, Artero V. Coordination polymer structure and revisited hydrogen evolution catalytic mechanism for amorphous molybdenum sulfide. Nat Mater 2016;15:640–6.
- [32] Baloglou A, Pritzi M, Pascher TF, Hartmann JC, Grutza M-L, Ončák M, Kurz P, Beyer MK. Proton transfer reactivity of molybdenum oxysulfide dianions [Mo₂O₂S₆]²⁻ and [Mo₂O₂S₅]₂₋: the role of Coulomb barriers. Int J Mass Spectrom 2021;464:116558.
- [33] Lee C-H, Lee S, Lee Y-K, Jung YC, Ko Y-I, Lee DC, Joh H-I. Understanding the origin of formation and active sites for thiomolybdate [Mo₃S₁₃]²⁻ clusters as hydrogen evolution catalyst through the selective control of sulfur atoms. ACS Catal 2018;8: 5221–7.
- [34] Xi F, Bogdanoff P, Harbauer K, Plate P, Höhn C, Rappich J, Wang B, Han X, van de Krol R, Fiechter S. Structural transformation identification of sputtered amorphous MoS_x as an efficient hydrogen-evolving catalyst during electrochemical activation. ACS Catal 2019;9:2368–80.
- [35] Li B, Jiang L, Li X, Cheng Z, Ran P, Zuo P, Qu L, Zhang J, Lu Y. Controllable synthesis of nanosized amorphous MoS_x using temporally shaped femtosecond laser for highly efficient electrochemical hydrogen production. Adv Funct Mater 2019:29
- [36] Ye Z, Yang J, Li B, Shi L, Ji H, Song L, Xu H. Amorphous molybdenum sulfide/ carbon nanotubes hybrid nanospheres prepared by ultrasonic spray pyrolysis for electrocatalytic hydrogen evolution. Small 2017;13:1700111.
- [37] Bose R, Balasingam SK, Shin S, Jin Z, Kwon DH, Jun Y, Min Y-S. Importance of hydrophilic pretreatment in the hydrothermal growth of amorphous molybdenum sulfide for hydrogen evolution catalysis. Langmuir 2015;31:5220–7.
- [38] Rahmatinejad J, Liu X, Zhang X, Raisi B, Ye Z. Embedding amorphous MoS_x within hierarchical porous carbon by facile one-pot synthesis for superior sodium ion storage. J Energy Chem 2022;75:240–9.
- [39] Reddy S, Du R, Kang L, Mao N, Zhang J. Three dimensional CNTs aerogel/MoS_x as an electrocatalyst for hydrogen evolution reaction. Appl Catal B Environ 2016;194: 16–21.
- [40] Guo X, Wang L, Zeng J, Shao Y, Cui W, Zhang C, Wang W, Hao C, Li G. Defect-rich MoS_x/carbon nanofiber arrays on carbon cloth for highly efficient electrocatalytic hydrogen evolution. Int J Hydrogen Energy 2018;43:23118–25.
- [41] Hu W-H, Shang X, Han G-Q, Dong B, Liu Y-R, Li X, Chai Y-M, Liu Y-Q, Liu C-G. MoS_x supported graphene oxides with different degree of oxidation as efficient electrocatalysts for hydrogen evolution. Carbon 2016;100:236–42.
- [42] Muthukumar K, Leban L, Sekar A, Elangovan A, Sarkar N, Li J. Tuning the defects in MoS₂/reduced graphene oxide 2D hybrid materials for optimizing battery performance. Sustain Energy Fuels 2021;5:4002–14.
- [43] Li Y, Wang H, Xie L, Liang Y, Hong G, Dai H. MoS₂ nanoparticles grown on graphene: an advanced catalyst for the hydrogen evolution reaction. J Am Chem Soc 2011;133:7296–9.
- [44] Anantharaj S, Ede SR, Karthick K, Sankar SS, Sangeetha K, Karthik P, Kundu S. Precision and correctness in the evaluation of electrocatalytic water splitting: revisiting activity parameters with a critical assessment. Energy Environ Sci 2018; 11:744–71.
- [45] Rajendran S, Sekar A, Li J. Mechanistic understanding of Li metal anode processes in a model 3D conductive host based on vertically aligned carbon nanofibers. Carbon 2023;212:118174.
- [46] Kudin KN, Ozbas B, Schniepp HC, Prud'homme RK, Aksay IA, Car R. Raman spectra of graphite oxide and functionalized graphene sheets. Nano Lett 2008;8: 36–41.
- [47] Vineesh TV, Sekar A, Rajappa S, Pal S, Alwarappan S, Narayanan TN. Non-precious metal/metal oxides and nitrogen-doped reduced graphene oxide based alkaline water-electrolysis cell. ChemCatChem 2017;9:4295–300.
- [48] Li H, Zhang Q, Yap CCR, Tay BK, Edwin THT, Olivier A, Baillargeat D. From bulk to monolayer MoS₂: evolution of Raman scattering. Adv Funct Mater 2012;22: 1385–90
- [49] Pimenta MA, del Corro E, Carvalho BR, Fantini C, Malard LM. Comparative study of Raman spectroscopy in graphene and MoS₂-type transition metal dichalcogenides. Accounts Chem Res 2015;48:41–7.
- [50] Vinoba M, Navvamani R, Al-Sheeha H. Controllable thermal conversion of thiomolybdate to active few-layer MoS₂ on alumina for efficient hydrodesulfurization. SN Appl Sci 2019;1:340.
- [51] Vrubel H, Hu X. Growth and activation of an amorphous molybdenum sulfide hydrogen evolving catalyst. ACS Catal 2013;3:2002–11.
- [52] Lide DR. CRC handbook of Chemistry and physics. 85th ed. New York: CRC Press; 2004.
- [53] Wang H, Lu Z, Kong D, Sun J, Hymel TM, Cui Y. Electrochemical tuning of MoS₂ nanoparticles on three-dimensional substrate for efficient hydrogen evolution. ACS Nano 2014;8:4940–7.
- [54] Anantharaj S, Karthik PE, Noda S. The significance of properly reporting turnover frequency in electrocatalysis research. Angew Chem Int Ed 2021;60:23051–67.